

1 Response of water vapour D-excess to
2 land-atmosphere interactions in a semi-arid
3 environment

4
5 Stephen D. Parkes¹, Matthew F. McCabe^{1,2}, Alan D. Griffiths³, Lixin Wang⁴, Scott Chambers³,
6 Ali Ershadi^{1,2}, Alastair G. Williams³, Josiah Strauss², Adrian Element³

7
8 ¹ Water Desalination and Reuse Centre, King Abdullah University of Science and Technology
9 (KAUST), Jeddah, Saudi Arabia

10 ² Department of Civil and Environmental Engineering, University of New South Wales, Sydney,
11 Australia

12 ³ Australian Nuclear Science and Technology Organization, Sydney, New South Wales,
13 Australia

14 ⁴ Department of Earth Sciences, Indiana University–Purdue University Indianapolis (IUPUI),
15 Indianapolis

16

17 Corresponding Author: Stephen Parkes, stephen.parkes@kaust.edu.sa

18 Keywords: Stable isotopes, D-excess, water vapour, land-atmosphere coupling

19

20 Key points:

- 21 • Examined the influence of local land-atmosphere coupling on water vapour isotopes
- 22 • Diurnal cycle of D-excess in water vapour is determined by an interplay between large
23 scale moisture sources and nocturnal processes
- 24 • The D-excess of the evaporation fluxes impose negative forcing on the ambient vapour
- 25 • Nocturnal D-excess values are determined by surface exchange and turbulent mixing

26 **Abstract**

27 The stable isotopic composition of water vapour provides information about moisture sources
28 and processes difficult to obtain with traditional measurement techniques. Recently, it has been
29 proposed that the D-excess ($d_v = \delta^2\text{H} - 8 \times \delta^{18}\text{O}$) of water vapour can provide a diagnostic tracer
30 of continental moisture recycling. However, D-excess exhibits a diurnal cycle that has been
31 observed across a variety of ecosystems and may be influenced by a range of processes beyond
32 regional scale moisture recycling, including local evaporation (ET) fluxes. There is a lack of
33 measurements of D-excess in evaporation (ET) fluxes, which has made it difficult to assess how
34 ET fluxes modify the D-excess in water vapour (d_v). With this in mind, we employed a chamber
35 based approach to directly measure D-excess in ET (d_{ET}) fluxes. We show that ET fluxes
36 imposed a negative forcing on the ambient vapour and could not explain the higher daytime d_v
37 values. The low d_{ET} observed here was sourced from a soil water pool that had undergone an
38 extended drying period, leading to low D-excess in the soil moisture pool. A strong correlation
39 between daytime d_v and locally measured relative humidity was consistent with an oceanic
40 moisture source, suggesting that remote hydrological processes were the major contributor to
41 daytime d_v variability. During the early evening, ET fluxes into a shallow nocturnal inversion

42 layer caused a lowering of d_v values near the surface. In addition, transient mixing of vapour
43 with a higher D-excess from above the nocturnal inversion modified these values, causing large
44 within night variability. These results indicate d_{ET} can generally be expected to show large
45 spatial and temporal variability and to depend on the soil moisture state. For long periods
46 between rain events, common in semi-arid environments, ET would be expected to impose
47 negative forcing on the surface d_v . **Spatial and temporal variability of D-excess in ET fluxes**
48 **therefore needs consideration for moisture recycling studies using d_v . In addition, during**
49 **extended dry periods with weak moisture recycling, D-excess may act as a tracer of the relative**
50 **humidity at the oceanic moisture source.**

51 **1 Introduction**

52 Climate change has the potential to significantly impact surface and atmospheric water budgets.
53 Our best understanding of future exchanges between the atmospheric water cycle and the land
54 surface on a regional to global scale, is likely to be gained through application of numerical
55 models (Decker et al. 2015; Evans and McCabe, 2010; Harding and Snyder, 2012; Wei et al.
56 2012). Consequently, continual improvement of available models is essential, but is contingent
57 upon ongoing validation and evaluation of model performance over a broad range of landscapes
58 and climate types (McCabe et al. 2016). **To do this effectively, a range of datasets that directly**
59 **quantify a variety of processes represented in these models are required (Jana et al., 2016).**
60 **Unfortunately, datasets that directly measure process level land-atmosphere exchanges are**
61 **limited.**

62 Water is composed of a number of stable isotopologues that have sufficient abundance to be
63 measured in atmospheric water vapour ($^1\text{H}_2^{16}\text{O}$, $^1\text{H}^2\text{H}^{16}\text{O}$, $^1\text{H}_2^{18}\text{O}$ and $^1\text{H}_2^{17}\text{O}$). The deviation of
64 the isotope ratios, reported as

$$65 \quad \delta = \left[\frac{R_{\text{sample}}}{R_{\text{VSMOW}}} - 1 \right] \text{‰} \quad (1)$$

66 where R is the isotope ratio ($^2\text{H}/^1\text{H}$ or $^{18}\text{O}/^{16}\text{O}$) and VSMOW (Vienna Standard Mean
67 Ocean Water) is the international standard for reporting water isotope ratios, have potential to
68 evaluate land-atmosphere exchange by discriminating processes based on their isotopic signature
69 (Berkelhammer et al. 2013; Lee et al. 2009; Noone et al. 2013; Risi et al. 2013). Isotopic ratios
70 of water vapour ($\delta^2\text{H}$ and $\delta^{18}\text{O}$) can therefore provide information that is either complimentary or
71 even unobtainable when using conventional measurement techniques.

72 **The utility of water isotope ratios for tracing sources of moisture derives from the characteristic**
73 **equilibrium and kinetic isotopic fractionation that occurs when water undergoes a phase change,**
74 **causing light water molecules to preferentially accumulate in the vapour phase.** Soil moisture is
75 typically enriched in heavy isotopes relative to the ocean (Gat, 1996), so water vapour derived
76 from land surface evaporation is expected to have a different isotopic composition to moisture
77 evaporated from the ocean. This has led to a number of studies using stable isotopes in
78 precipitation to partition oceanic and land derived sources (Froehlich et al. 2008; Tian et al.
79 2001). However, land-atmosphere exchange is not restricted to periods of precipitation, and there
80 are relatively few studies examining the role of land-atmosphere exchange on ambient humidity
81 budgets using stable isotope observations of vapour (e.g. Aemisegger et al. 2014; Risi et al.
82 2013).

83 In addition to the source of moisture, the magnitude of isotopic fractionation that occurs when
84 water evaporates is related to the liquid surface temperature and humidity gradient between the
85 evaporating surface and atmosphere (Craig and Gordon, 1965). The temperature dependent
86 equilibrium exchange between liquid and vapour is the largest contributor to isotopic
87 fractionation during evaporation, with the fractionation for $\delta^2\text{H}$ approximately a factor of 8
88 greater than $\delta^{18}\text{O}$. The effect of kinetic fractionation associated with moisture diffusing from the
89 thin laminar layer of vapour in equilibrium with the water surface to the turbulent atmosphere
90 above is influenced by the relative humidity of the atmosphere and wind speed (Merlivat and
91 Jouzel, 1979). The kinetic fractionation factors for $\delta^2\text{H}$ and $\delta^{18}\text{O}$ are similar, causing the ratio of
92 $\delta^2\text{H}$ to $\delta^{18}\text{O}$ in the evaporating vapour to decrease as kinetic effects increase with decreasing
93 relative humidity. This phenomenon has been observed for evaporative conditions over the
94 Mediterranean sea (Gat et al. 2003; Pfahl and Wernli, 2009) and the Great Lakes in Northern
95 USA (Gat et al. 1994; Vallet-Coulomb et al. 2008).

96 The D-excess parameter ($\text{D-excess} = \delta^2\text{H} - 8 \times \delta^{18}\text{O}$) (Dansgaard, 1964), quantifies the non-
97 equilibrium isotopic fractionation. A reproducible relationship between the D-excess and relative
98 humidity near the ocean surface has been observed across a wide range of locations (Kurita,
99 2011; Pfahl and Wernli, 2008; Steen-Larsen et al. 2015; Uemura et al. 2008). **Therefore**, it has
100 been suggested that for precipitation, D-excess is a good tracer of sea surface evaporative
101 conditions (Masson-Delmotte et al. 2005; Merlivat and Jouzel, 1979). However, this view has
102 recently been challenged due to the role local and regional scale land-atmosphere coupling has in
103 modifying the D-excess of atmospheric humidity over diurnal (Lai and Ehleringer, 2011;
104 Simonin et al. 2014; Welp et al. 2012; Zhao et al. 2014) and synoptic timescales (Aemisegger et

105 al. 2014). As evidence for the role ET plays in modifying the D-excess of water vapour (d_v), a
106 diurnal cycle of d_v near the land surface across a range of land surface types has been observed
107 (Berkelhammer et al. 2013; Simonin et al. 2014; Welp et al. 2012). The diurnal cycle shows
108 higher values in the day, which has been proposed to be driven by entrainment (Lai and
109 Ehleringer, 2011; Welp et al. 2012), local evapotranspiration sources (Simonin et al. 2014; Zhao
110 et al. 2014) and meteorological conditions affecting the D-excess of the evaporative fluxes (d_{ET})
111 (Welp et al. 2012; Zhao et al. 2014), coupled with low nocturnal values resulting from
112 equilibrium exchange between liquid and vapour pools (Simonin et al. 2014) and dew fall
113 (Berkelhammer et al. 2013). For synoptic scales, Aemisegger *et al.* (2014) showed that moisture
114 recycling from the land surface had a significant impact on d_v for *in-situ* measurements in
115 Switzerland. These studies have largely relied on isotopic models to assess the contribution of
116 ET fluxes, but a lack of d_{ET} measurements make it difficult to draw robust conclusions.

117 The evidence provided by these studies suggest d_v is a tracer of moisture recycling both on
118 diurnal and synoptic time scales, and is influenced by dynamics of surface moisture budgets in
119 the atmospheric boundary layer (ABL). However, as noted by Welp *et al.* (2012), ET and
120 entrainment fluxes both increase as the ABL grows through the previous days residual layer,
121 which can make interpreting the role of local moisture recycling on d_v difficult. To overcome
122 this, Simonin *et al.* (2014) used a trajectory model to simulate the D-excess of vapour evaporated
123 over the ocean. As the d_v was greater than the modelled oceanic moisture source, it was assumed
124 that high daytime values were supported by local ET fluxes. Zhao *et al.* (2014) suggested that
125 since, on cloudy days, no diurnal cycle was observed for the d_v , that ET fluxes played a dominant
126 role. Whilst these studies provide compelling evidence for the role of ET driving the diurnal

127 cycle of d_v , no measurements of d_{ET} were made. To date the only measurements of d_{ET} have been
128 presented by Huang *et al.* (2014) over a maize crop in north west China. Interestingly, their
129 direct measurements conflicted with previous interpretations and showed that the d_{ET} invoked a
130 negative forcing on d_v , even though a strong diurnal cycle of high values in the day and low
131 values at night were observed. In order to better interpret the role of local moisture recycling on
132 the diurnal cycle of d_v , measurements of d_{ET} are required to assess if the negative forcing is
133 consistent in different ecosystems.

134 The aim of this work is to provide much needed d_{ET} measurements to investigate how ET fluxes
135 modulate the d_v diurnal cycle. To do this, chamber based measurements of the ET flux isotopic
136 compositions were combined with *in-situ* measurements of water vapour isotope ratios,
137 meteorological and radon concentration observations. The data was collected in a region of the
138 semi-arid Murray Darling basin in south-eastern Australia. These data represent the first such
139 collection of the $\delta^2\text{H}$, $\delta^{18}\text{O}$ and D-excess in water vapour from this region of Australia. The
140 augmentation of the chamber based measurements with in-situ observations provide a framework
141 to directly assess the role local ET fluxes **have** on ambient vapour D-excess.

142 **2 Methods**

143 **2.1 Site Description**

144 During the austral autumn of 2011, a field campaign covering the period April 27 to May 11 was
145 conducted at the Baldry Hydrological Observatory (BHO) (-32.87, 148.54, 460 m above sea
146 level) located in the central-west of New South Wales, Australia (Figure 1). The climate of the
147 region is characterised as semi-arid with no clear wet season, a mean annual rainfall of 600 mm,
148 and a mean annual temperature of 24.2°C (source Australian Bureau of Meteorology, 2015,

149 <http://www.bom.gov.au/>). The BHO grassland flux tower was the central site of measurements
150 and was located in a natural grassland paddock of dimensions approximately 900m (north-south)
151 by 300m (west-east), with a gentle slope decreasing in elevation by approximately 20 m from
152 southeast to northwest. The flux tower was located 650 m from the road to the south and 200 m
153 from a reforested paddock to the west. The forest site to the west and southwest was reforested in
154 2001 with *Eucalyptus camaldulensis*, *Eucalyptus crebra* and *Corymbia maculate*. At the time of
155 the campaign these trees were approximately 10 m tall. All other adjacent paddocks and most of
156 the surrounding region had similar surface characteristics to the grassland measurement site.

157 **2.2 Water stable isotope analyses**

158 **2.2.1 *In-situ* water vapour calibration and sampling**

159 In-situ water vapour isotope ratios were monitored using a Wavelength Scanning Cavity Ring
160 Down Spectrometer (WS-CRDS L115-I, Picarro Inc., Sunnyvale, CA, USA), while flux
161 chambers were interfaced to an Off Axis Integrated Cavity Output Spectrometer (OA-ICOS,
162 DLT100, Los Gatos Research (LGR), Mountain View, CA, USA) to determine the isotopic
163 composition of ET fluxes. Using an automated continuous flow calibration system (built in-
164 house), we simultaneously determined calibration coefficients for both analysers. Calibration
165 experiments were designed to determine the water vapour mixing ratio cross-sensitivity of
166 isotope ratios and linearity of the $\delta^2\text{H}$ and $\delta^{18}\text{O}$ measurements. Due to logistical constraints, the
167 calibration system was not transported into the field, so corrections were determined by
168 compositing multiple calibration experiments run before and after the campaign.

169 During the campaign, a second portable calibration system was employed to monitor time
170 dependent drift of the Picarro analyser (CTC HTC-Pal liquid autosampler; LEAP Technologies,

171 Carrboro, NC, USA). Two standards spanning expected water vapour $\delta^2\text{H}$ (-49.1 and -221.9‰)
172 and $\delta^{18}\text{O}$ (-9.17 and -27.57‰) ranges were injected at approximately 18 mmol.mol⁻¹ on three
173 occasions during the campaign.

174 The uncertainty of measurements from both isotopic analysers was estimated by applying mixing
175 ratio cross-sensitivity and linearity corrections to all calibration measurements collected prior,
176 during and after the campaign. For the Picarro instrument, measurement uncertainty was 0.8, 0.2
177 and 1.9‰ for $\delta^2\text{H}_v$, $\delta^{18}\text{O}_v$ and d_v , respectively. No calibrations were performed for the LGR in
178 field, so the measurement uncertainty was estimated by compositing calibration measurements
179 made before and after the campaign, which was 0.9, 0.4 and 3.3‰ for $\delta^2\text{H}$, $\delta^{18}\text{O}$ and d_v .

180 Although no calibration experiments were run on the LGR during the campaign, simultaneous
181 *in-situ* measurements were made with the Picarro when chamber measurements were not
182 operated. During the day, average differences and standard deviations (1σ) of these differences
183 were -0.06 (± 2.0), 0.13 (± 0.5) and 0.4 (± 3.3) ‰ for $\delta^2\text{H}$, $\delta^{18}\text{O}$ and d_v , respectively. A comparison
184 of the analysers is shown in supplementary section S1. At night, while the Picarro was able to
185 maintain a steady cavity and optical housing temperature, the LGR cavity temperature dropped
186 by up to 8°C. In response to the drop in cavity temperature, night time LGR measurements of
187 $\delta^{18}\text{O}$ and d_v and to a lesser extent the $\delta^2\text{H}$, were physically unrealistic and discarded from
188 subsequent analyses. Chamber measurements were therefore restricted to between 09:00 (when
189 the LGR cavity temperature had stabilised and *in-situ* measurements were again in agreement
190 with the Picarro) and 17:00 (before LGR cavity temperatures began dropping).

191 A schematic diagram illustrating the sampling design for water vapour is shown in Figure 2.
192 Half-hourly vertical profiles of humidity and isotopes were sampled by drawing air to the *in-situ*
193 analyser through 10 mm O.D. PTFE tubing, located at 5 heights on a 7.5 m tower (0.5, 1, 2, 5
194 and 7.5 m Above Ground Level). The instrument was interfaced to a 5 inlet manifold that
195 enabled sequential sampling of the different heights. **Approximately 20 m of tubing was required**
196 **to connect the tower inlet to the analyser. A vacuum pump (MV 2 NT, Vacuubrand, Wertheim,**
197 **Germany) was used to draw air through all inlets to the analyser at a flow rate of 10 l.min⁻¹.** To
198 avoid condensation, sample tubes and intakes were wrapped in 15 W m⁻¹ heat tape, insulated by
199 Thermobreak pipe and placed inside 100 mm PVC pipe. The sample tube temperature was
200 controlled using a Resistance Thermometer Detector (RTD) coupled to a CAL3300 temperature
201 controller (CAL controls Ltd., Grayslake, IL, USA). The inlets at each height were constructed
202 from inverted funnels with mesh filters. In this study we present block hourly averages of all
203 measurements collected at all heights.

204 **2.2.2 Flux chambers**

205 To separate the isotopic signatures of the ET flux components, flux chambers were deployed on
206 both bare soil and vegetated plots to determine the isotopic signature of the evaporative fluxes.
207 An open chamber was designed with a high volume to footprint ratio to avoid the chamber
208 mixing ratio rapidly reaching the dew point temperature (causing condensation) and to minimise
209 impacts on the evaporation environment. A schematic of the chamber design is shown in Figure
210 3. Four flanged metal collars were inserted ~10 cm into the soil column two days before the
211 beginning of the campaign. **While this was a short settling time for chamber bases, shallow roots**
212 **of grass cover within the chamber were largely unaffected.** All vegetation was removed from

213 bare soil plots when the metal collars were inserted into the soil. A single chamber cover was
214 constructed of 4 mm G-UVT Plexiglass (Image Plastics, Padstow, Australia), selected for its
215 higher transmittance of UV and blue light. The dimensions of the chamber were 0.1 x 0.1 x 0.8
216 m (width x length x height), with the inlets and outlets at 0.1 and 0.7 m above the surface,
217 respectively. All sampling tube was 10 mm PTFE. The inlet to the chamber was connected to
218 tubing that drew in air from 1.5 m above the ground surface. The outlet was connected to a
219 flowmeter (VFA-25, Dwyers, Michigan City, IN, USA) that regulated the air flow at 10 L.min⁻¹
220 and was driven by a two-stage diaphragm pump. A T-piece was connected to the LGR, which
221 bled off the required air flow. All tubing between chamber and the analyser were wrapped in
222 heating tape (15 W m⁻²) and foam insulation. **High flow rates were used to combat memory**
223 **effects modifying the isotopic composition of the vapour within the chamber. Analysis of**
224 **chamber measurements were conducted on 2-5 minutes of data, so 2.5-6.25 chamber volumes**
225 **were exchanged.**

226 To monitor the internal chamber environment, an air temperature and humidity probe (HMP155,
227 Vaisala, Vantaa, Finland) was mounted inside the chamber. To monitor the attenuation of the
228 incoming radiation by the chamber, photosynthetic flux density was measured (LI-190R, Licor,
229 Lincoln, NE, USA) inside and outside the chamber. Ten second averages of the temperature,
230 relative humidity and photosynthetic flux density were stored in a datalogger (CR1000,
231 Campbell Scientific, Logan, UT, USA). In the supplementary section S2 we use these ancillary
232 measurements to assess the impact of observed changes in chamber environment on the isotopic
233 composition of the ET flux. The largest contributor to uncertainty caused by changing the

234 evaporative environment was the temperature, although these affects were small compared to the
235 overall variability of the chamber derived ET isotopic compositions.

236 **2.2.3 Isotopic composition of ET flux from chamber measurements**

237 Mass balance or Keeling mixing (Keeling, 1958; Wang et al. 2013) models have been applied to
238 determine the isotopic composition of ET fluxes from chamber measurements (Lu et al., 2016;
239 Wang et al., 2013b). The focus of this work was not to evaluate chamber measurement
240 techniques and considering it has been shown that Keeling and mass balance methods give very
241 similar results, we focus on using the Keeling mixing model, given by:

$$242 \delta_{chamber} = q_{BG} \frac{(\delta_{BG} - \delta_{ET})}{q_{chamber}} + \delta_{ET} \quad (2)$$

243 where q_{BG} is the water vapour mixing ratio entering the chamber through the inlet and
244 δ_{BG} its isotopic composition, $q_{chamber}$ is the mixing ratio in the chamber and δ_{ET} is the isotopic
245 composition of the ET flux. The δ_{ET} is determined from the intercept of $\delta_{chamber}$ against $1/q_{chamber}$.
246 A key assumption of the Keeling method is that the isotopic composition of the background
247 vapour and the evaporation flux remain constant during the chamber measurements. For chamber
248 measurements longer than 5 minutes, non-linear Keeling plots were commonly observed,
249 indicating a change in isotopic composition of one of the sources of vapour. We therefore
250 restricted the Keeling analysis to a maximum of 5 minutes after an increase in the concentration
251 was observed by the analyser. Ensuring the linearity of Keeling plots also ensured that the
252 influence of memory effects was minimised. Memory effects would constitute an additional
253 moisture source, violating the two source assumption of the Keeling methods and reducing
254 Keeling plot linearity. The analysis was also restricted to periods where the H₂O mixing ratio

255 was increasing, so analysis was generally performed on 2-5 minutes of data. In addition, only
 256 chamber measurements where the correlation between δ_{chamber} and $1/q_{\text{chamber}}$ was significant
 257 ($p < 0.001$) were included in this analysis. A few chamber measurements where obvious non-
 258 linearity or very small changes in q_{chamber} occurred were also subjectively removed. Of a total of
 259 105 chamber measurements made from the 4 vegetation plots during the campaign, 99
 260 measurements of the $\delta^2\text{H}_{\text{ET}}$, and 97 measurements of $\delta^{18}\text{O}_{\text{ET}}$ and d_{ET} were retained. For the bare
 261 soil plots, 84 of the 86 chamber measurements were retained for the $\delta^2\text{H}_{\text{ET}}$, and 77 of the $\delta^{18}\text{O}_{\text{ET}}$
 262 and d_{ET} . The eight plots were sampled 2 to 4 times each day on all days except the first two days
 263 of the campaign, and the 2nd and 5th of May. Sampling was restricted to between 9:00 and 17:00
 264 LST (local solar time) as the large temperature dependence of the LGR at low ambient
 265 temperatures limited the accuracy of the chamber measurements.

266 Results from vegetated plots were used to determine ET flux isotopic compositions and
 267 determine how ET influences d_v . The bare soil plots were used to determine the isotopic
 268 composition of soil evaporation fluxes and to provide an estimate of the isotopic composition of
 269 water at the evaporation front. The isotopic composition of the water at the evaporation front (δ_L)
 270 was determined by rearranging the Craig and Gordon model:

$$271 \quad \delta_L = \frac{\delta_E(1-RH)+RH \delta_A+\varepsilon+\varepsilon_k}{\alpha} \quad (3)$$

272 where the isotopic composition of the evaporation flux (δ_E) is taken from the bare soil
 273 chamber measurements, relative humidity (RH) normalised to the surface temperature
 274 determined from infrared surface temperature measurements (section 2.3), and the ambient
 275 vapour isotope composition (δ_A) determined from Picarro *in-situ* measurements. Equilibrium

276 fractionation and enrichment factors (α , $\epsilon=(\alpha-1)\%$) were calculated from the surface temperature
277 measurements using the equations of Horita and Wesolowski (1994), while the kinetic
278 enrichment factor (ϵ_k) was determined as in Gat (1996), but using the parameterisation of the
279 exponent of the diffusion coefficients described by Mathieu and Bariac (1996) and the diffusion
280 coefficients determined by Merlivat (1978).

281 **2.2.4 Isoforcing of ET**

282 The isotopic composition of the near-surface atmospheric water vapour is modified by surface
283 ET fluxes. The impact of ET fluxes on surface vapour isotopes varies over diurnal timescales
284 with the strength of vertical mixing in the ABL or over synoptic timescales as background
285 moisture conditions change. The magnitude and isotopic composition of the ET flux as well as
286 the amount of water vapour in the atmosphere also have an influence. The ET isoforcing (I_{ET})
287 represents a useful quantity to study the influence of ET fluxes on the surface vapour and is
288 defined as:

$$289 \quad I_{ET} = \frac{F_{ET}}{H_2O} (\delta_{ET} - \delta_A) \quad (8)$$

290 where F_{ET} is the ET flux in $\text{mol}\cdot\text{m}^{-2}\cdot\text{s}^{-1}$, H_2O is the ambient mixing ratio in $\text{mol}\cdot\text{air}\cdot\text{mol}^{-1}$
291 H_2O^{-1} measured by the local meteorological tower, and δ_{ET} and δ_A are the isotopic compositions
292 of the evaporation flux and ambient water vapour, respectively (Lee et al. 2009).

293 For each chamber measurement, a surface isoforcing was calculated for $\delta^2\text{H}$, $\delta^{18}\text{O}$ and D-excess
294 from the determined ET isotopic composition, the hourly averaged ET flux, mixing ratio and δ_A
295 values. The importance of surface fluxes modifying surface vapour isotope composition was
296 investigated for diurnal and synoptic timescales.

297 **2.2.5 Plant and soil sampling**

298 Grass samples were collected three times a day for the duration of the campaign. They were
299 sampled randomly within 100 m of the instrumentation. Each sample consisted of approximately
300 10 grass leaves, which were placed in 12ml Exetainer vials (Labco, Ceredigion, UK). The grass
301 samples were assumed to represent bulk leaf water. Soil samples were collected every 2 days
302 throughout the campaign by sampling from the top 5cm of the soil column. They were collected
303 in 50ml glass bottles. Soil and plant samples were stored in a fridge (4°C), before using distilled
304 using the method of West *et al.* [2006] and analysed on a Delta V Advantage Isotope Ratio Mass
305 Spectrometer (Thermo Fisher Scientific Corporation, Massachusetts, United States). For $\delta^2\text{H}$
306 analysis, water samples were introduced into a H-Device containing a chromium reactor, while
307 for the $\delta^{18}\text{O}$ analysis, water samples were equilibrated with CO_2 on a Gas Bench II
308 chromatography column (Thermo Fisher Scientific Corporation, Massachusetts, USA) before
309 being transferred to the IRMS for analysis.

310 **2.3 ET Fluxes and Meteorological measurements**

311 An eddy covariance system comprising a Campbell Scientific 3D sonic anemometer (CSAT-3,
312 Campbell Scientific, Logan, UT, USA) along with a LiCOR 7500 (Li-7500, LiCor Biosciences,
313 Lincoln, NB, USA) analyser was installed at an elevation of 2.5 m. The system was located
314 approximately 10 m from the stable isotope observation tower and sampled at 10 Hz, with flux
315 averages output at 30 minute intervals. The ET fluxes from the eddy covariance tower are used
316 to quantify the isoforcing of ET on the overlying atmosphere.

317 A meteorological tower was co-located with the eddy covariance system, acting as an aid for
318 interpretation of measurements. The tower comprised a Kipp and Zonen CNR4 radiometer,

319 Apogee infrared surface temperature, RIMCO rain gauge, Vaisala HMP75C temperature and
320 humidity probe, RM Young wind sentry (wind speed and direction), Huskeflux ground heat flux
321 plate and Vaisala BaroCap barometric pressure sensor. Both meteorological tower data and
322 eddy-covariance data were inspected visually to detect and remove spikes. The low-frequency
323 eddy covariance data (30 minute resolution) were corrected for coordinate rotation (Finnigan et
324 al. 2003) and density effects (Leuning, 2007) using the PyQC software tool (available from
325 code.google.com/p/eddy).

326 **2.4 Radon-222 measurements**

327 The naturally occurring radioactive gas radon (^{222}Rn) is predominantly of terrestrial origin and
328 its only atmospheric sink is radioactive decay (Zahorowski et al. 2004). The surface flux density
329 of radon is relatively constant in space and time, and since the half-life is much greater than ABL
330 mixing timescales, it is an ideal tracer of vertical mixing strength within the ABL (Chambers et
331 al. 2014; Griffiths et al. 2013; Williams et al. 2010). Hourly radon concentrations were measured
332 by an Alpha Guard (Saphymo GmbH, Frankfurt, Germany) placed in a ~20 L enclosure. The
333 enclosure was purged at $\sim 15 \text{ L}\cdot\text{min}^{-1}$ with a vacuum pump (2107 Series, Thomas, Wisconsin,
334 USA) that sampled from a height of 2 m through 10 mm O.D. PTFE tubing. Radon
335 measurements were used to aid the interpretation of the diurnal variations in vertical mixing (see
336 Griffiths et al. 2013).

337 **3 Results**

338 **3.1 Meteorological observations**

339 The two-week campaign was conducted under predominantly calm meteorological conditions.
340 The last rain event was 10 days prior to the campaign, after which clear skies saw the soil

341 moisture decline towards minimum values observed for the site (Figure 4). In the middle of the
342 campaign (May 2nd), a cold front moved across south eastern Australia producing cloudy
343 conditions and 1.4 mm of precipitation at the site. No change in soil moisture was observed
344 following the rain event over the 0-10 cm soil layer.

345 Wind directions were variable during the campaign (see figure S3 and S4). Figure S4 shows
346 dominant daytime wind directions were mainly from the east from 27th to 30th April, and from
347 the south after May 3rd, except on the 7th and 8th when the wind was from the west with a fetch
348 from the adjacent forest. At other times the fetch did not include the forested site. Daily
349 maximum temperatures on clear days ranged from 16 to 23°C, whilst night time minimum
350 temperatures fell to between 8 and -4°C. From May 7th onwards nocturnal temperatures fell
351 below zero. On clear nights the surface temperature fell below dew point temperature, indicating
352 dew fall. Apart from the night of the 27-28th April and the cloudy nights between 1st and 3rd
353 May, the surface temperature fell below dew point temperature and dew or frost was observed in
354 the morning, although heavier from the 7th May onwards.

355 Radon concentrations were low during the day, when the convective boundary layer reached its
356 maximum height, and high at night when radon emissions were confined within a shallow
357 nocturnal boundary layer. The accumulation at night was variable reflecting the degree of
358 nocturnal stability, mixing depth and occurrence of transient mixing events (Griffiths et al.
359 2013). There was general agreement between high nocturnal radon concentrations and low wind
360 speeds, but no direct relationship. The lack of a direct relationship indicates that radon can
361 provide additional information about nocturnal mixing and surface exchange that compliments
362 standard meteorological measurements (Chambers et al. 2015a, 2015b; Williams et al. 2013).

363 ET fluxes were in general quite low, reflecting the low soil moisture content. The ET flux did
364 show a marked increase the day after the small rain event on May 2nd and noticeably smaller
365 fluxes were observed following deterioration of grass health in response to frost formation (
366 from May 7th).

367 **3.2 Relationship between $\delta^2\text{H}$ and $\delta^{18}\text{O}$ of the different water pools**

368 A summary of the isotopic composition of all observed and modelled water pools are presented
369 in Figure 6. The local MWL (Hughes and Crawford, 2013) is to the left of the global MWL
370 (Craig, 1961), illustrating the regions characteristically high precipitation D-excess (Crawford et
371 al., 2013). Ambient vapour observations aligned closely with the local MWL, but with a
372 distribution that lying left and right of the local MWL. Alignment between observations and the
373 MWL show that equilibrium fractionation was the dominant process modifying $\delta^2\text{H}$ and $\delta^{18}\text{O}$ in
374 water vapour, while non-equilibrium kinetic processes shift observations away from the MWL
375 that are more readily observed for d_v measurements.

376 Plant and soil water pools were enriched relative to the vapour and distributed to the right of the
377 MWL, indicating evaporative enrichment. Soil water isotopes at the evaporation front (δ_L) were
378 very enriched and had lower D-excess values (mean and standard deviations (1σ) were 50 ± 12 ,
379 31 ± 3.8 and -131 ± 22 ‰ for $\delta^2\text{H}$, $\delta^{18}\text{O}$ and D-excess) relative to the average soil moisture
380 between 0 and 5 cm (mean and standard deviations (1σ) were -15 ± 4.2 , 2.6 ± 2.5 and -36 ± 17 ‰
381 for $\delta^2\text{H}$, $\delta^{18}\text{O}$ and D-excess). **Low D-excess and enriched isotopes indicated large evaporative**
382 **enrichment under non-equilibrium conditions, consistent with $\delta^{18}\text{O}$ soil profile measurements of**
383 **Dubbert *et al.*, (2013) and $\delta^2\text{H}$ profiles of Allison *et al.*, (1983). The uncertainty of modelled**
384 **isotope values was most sensitive to parameterisation of the Craig-Gordon model. Changing the**

385 diffusion coefficient exponent (n) had the greatest impact on modelled soil water ($n=0.66$, $\delta^2\text{H} =$
386 42.7 ± 12 , $\delta^{18}\text{O} = 21.8\pm 3.8$ and $\text{D-excess} = -130.8\pm 22$ ‰). However, changing parameterisation
387 did not change the conclusion that soil moisture at the evaporation front was heavily enriched
388 with very low D-excess values.

389 ET flux isotopic compositions from vegetated chambers were enriched relative to vapour and
390 distributed to the right of the MWL (slope = 3.2). Similar isotopic compositions were measured
391 for bare soil and vegetated chambers. Mean and standard deviations (1σ) for vegetated and soil
392 chambers were $-47.1 (\pm 13)$ and $-50.2 (\pm 11)$ for $\delta^2\text{H}$, $-5.03 (\pm 3.8)$ and $-6.3 (\pm 2.7)\text{‰}$ for δ^{18} , and -
393 $6.3 (\pm 23)$ and $-0.12 (\pm 15)\text{‰}$ for D-excess, respectively. The similar ET isotopic composition
394 from bare soil and vegetated chambers could indicate soil evaporation was the dominant process
395 contributing to total ET. However, as pointed out in the discussion (section 4.3), the soil
396 evaporation source becomes progressively enriched (and D-excess lower) after a rain event,
397 which leads to convergence of soil evaporation and transpiration isotope compositions and
398 difficulties in identifying the dominant process from these observations. Nevertheless,
399 progressive reduction of D-excess of moisture at the evaporation front and to a lesser extent the
400 0-5cm layer, led to low d_{ET} relative to d_v and consequently ET to impose a negative isoforcing on
401 d_v .

402 Temporally, a clear trend was not observed for ET isotopic compositions over the measured
403 portion of the diurnal cycle or over the campaign. No measurements were made at night or
404 during the rapidly changing conditions of the morning transition, which may have led to our data
405 missing observed changes in ET isotope compositions during this time period.

406 3.3 *In-situ* water vapour isotopes and ET isoforcing

407 Observed H₂O mixing ratios and stable isotope compositions are shown in Figure 7. $\delta^2\text{H}$ and
408 $\delta^{18}\text{O}$ variability was similar, reflecting changes in both the synoptic and local meteorology. Prior
409 to the rain event (May 2nd), relatively moist conditions (**higher H₂O mixing ratios**) were
410 observed as air was transported from warmer ocean off the east coast of Australia (see wind
411 direction in figure S4). After May 5th, transport of air masses from the colder sea surface south
412 of continental Australia brought drier conditions to the site (**lower H₂O mixing ratios**). Moisture
413 source regions were confirmed by backward air trajectories calculated using the Stochastic Time-
414 Inverted Lagrangian Transport Model (STILT; Lin *et al.* (2003) not shown). These two time
415 periods are hereinafter referred as “wet period” (before May 2nd) and “dry periods” (after May
416 5th). The wet period coincided with more enriched isotopes and less diurnal variability. In the
417 dry period, a reproducible diurnal cycle for $\delta^2\text{H}$ and $\delta^{18}\text{O}$ was observed (see Figure 8),
418 characterised by a sharp increase at sunrise before decreasing from mid-morning (when vertical
419 mixing increased) until the next sunrise. These observations emphasise the complex relationship
420 between stable isotope observations in water vapour and both local and synoptic scale
421 meteorology.

422 The d_v dataset showed a robust diurnal cycle of high values in the day and low values at night,
423 consistent with what has been observed across a growing number of locations (Bastrikov *et al.*,
424 2014; Berkelhammer *et al.*, 2013; Huang and Wen, 2014; Simonin *et al.*, 2014; Welp *et al.*, 2012;
425 Zhao *et al.*, 2014). Wet period daytime d_v values were on average lower than those observed for
426 the dry period. Nocturnal d_v was lower during the night, but variable from night to night and
427 within individual nights, with no clear difference observed between wet and dry periods.

428 Contrasting daytime measurements of wet and dry periods indicate a role of large scale
429 processes, whilst the lack of contrast for nocturnal observation show the importance of local
430 processes.

431 The I_{ET} was always positive for δ^2H and $\delta^{18}O$ and mostly negative for D-excess and showed
432 large variability across individual days (Figure 7). I_{ET} was most sensitive to the magnitude of the
433 ET fluxes, producing the greatest forcing on ambient vapour in the middle of the day. However,
434 as the I_{ET} time series did not correspond to temporal variability of vapour δ^2H , $\delta^{18}O$ or D-excess,
435 in general the role of ET in modifying surface vapour isotope ratios was limited.

436 The level of agreement between the analysers presented some uncertainty for calculation of the
437 D-excess isoforcing. The sign of the isoforcing is dependent on the difference between d_v and d_{ET}
438 (equation 8). In some cases differences were small and within the range of agreement between
439 the two analysers. While this caused problems for accurate calculation of the absolute values of
440 D-excess isoforcing, for all chamber measurements passing our QC requirements, D-excess
441 decreased with concentration. This indicates that for all measurements, the D-excess isoforcing
442 was negative.

443 **3.4 Relationship between water vapour isotopes and local meteorology**

444 The relationships between local meteorological variables and water vapour isotopes were
445 examined to interpret the role of local processes (Table 1). Regression statistics are shown for
446 hourly observations and average daytime values (between 11:00 and 16:00 LST). Selecting
447 daytime measurements removes variability associated with transition between the stable
448 nocturnal and daytime convective boundary layer, and nocturnal periods when local surface

449 equilibrium exchange and dewfall affect vapour isotope compositions. Correlations determined
450 using only measurements in the middle of the day therefore provide a better indicator of how
451 local meteorology and ET isotopic composition modified ambient water vapour isotope ratios
452 from day to day.

453 Correlations calculated with hourly data were weak for $\delta^{18}\text{O}$ and $\delta^2\text{H}$. Only correlations with air
454 temperature ($R^2=0.24$ and 0.04 , respectively) and mixing ratio ($R^2=0.2$ for both isotopes) were
455 significant for both isotopes, and RH for $\delta^2\text{H}$ ($R^2=0.09$). For daytime observations, only $\delta^2\text{H}$
456 showed a significant correlation with daytime I_{ET} ($R^2=0.45$, $p<0.05$), but the slope was negative
457 in contrast to positive isoforcing. The weak relationships with local meteorology indicate the
458 greater importance of larger scale precipitation processes and atmospheric mixing occurring as
459 moisture was transported to the site.

460 As the diurnal cycle for d_v was consistent with growth and decay of the ABL, strong
461 relationships were observed with air temperature and RH for hourly observations. While the
462 local air temperature and RH could modify d_{ET} on diurnal timescales and in turn local d_v , the
463 chamber measurements showed relatively constant d_{ET} . These correlations therefore result from
464 the coincident diurnal variation of the d_v , RH and air temperature.

465 Daytime average d_v showed significant correlations with the air temperature, RH, ET flux and
466 mixing ratio. The relationship with ET fluxes was weak ($R^2=0.3$) and positive, but as negative D-
467 excess isoforcing was observed, a negative relationship would be expected. Likewise, the slope
468 between air temperature and d_v was negative, counter to what theory would predict for local or
469 remote moisture sources. The strongest relationship was observed with daytime RH ($R^2 = 0.74$),

470 which had a negative slope ($-0.52\%.\%^{-1}$) consistent with an inverse relationship between d_v and
471 RH for a large unchanging evaporation source. The strong relationship of d_v with the daytime
472 RH could indicate an important role for the evaporation conditions at remote moisture sources,
473 as is discussed below (Section 4.2).

474 **3.5 Diurnal variability of vapour isotopes**

475 Diurnal composites were divided into dry and wet periods and are shown in Figure 8. At sunrise
476 (approximately 06:30 LST) surface heating initiated vertical mixing, shown by the Radon
477 concentration maximum, causing temperature and ET flux to increase and RH decrease. Weak
478 vertical mixing immediately after sunrise and injection of ET into the still shallow surface layer
479 caused near-surface humidity to increase. Similarly for $\delta^2\text{H}$ and $\delta^{18}\text{O}$, the observed spike
480 immediately after sunrise was likely caused by ET fluxes with an enriched heavy isotope
481 composition, possibly from re-evaporation of dewfall. During the dry period, vapour $\delta^2\text{H}$ and
482 $\delta^{18}\text{O}$ increased more steeply, caused by the combination of a shallower surface layer observed at
483 the start of the morning transition, shown by higher Radon concentrations, and more dewfall on
484 the surface providing a greater initial evaporation source. Rapidly decreasing Radon
485 concentrations during this morning ABL transition caused by vigorous vertical mixing entraining
486 air from the residual layer of the previous day diluted ET fluxes and caused the $\delta^2\text{H}$, $\delta^{18}\text{O}$ and the
487 mixing ratio to first stabilise and then decrease. ET fluxes rapidly increased as the ABL grew,
488 but were not large enough to offset the dilution by dry air being mixed down from above or stop
489 depletion of surface $\delta^2\text{H}$ and $\delta^{18}\text{O}$.

490 The d_v also increased after sunrise, but aligned more closely with when strong vertical mixing
491 commenced, shown by the close agreement with Radon concentrations. The D-excess isoforcing

492 was negative, evidence that d_v increased from encroachment mixing as the new mixed layer grew
493 in depth and not ET fluxes. The dry period showed a greater d_v increase during the morning
494 transition, likely the result of higher d_v in background water vapour and greater differences
495 between the d_v of the residual and nocturnal layers.

496 In the afternoon, as solar insolation decreased, ET declined, convective mixing decayed, and d_v
497 decreased back to values similar to observed prior to sunrise. Radon shows how reduction in
498 vertical mixing causes the concentration of tracers emitted from the surface to increase. So while
499 ET decreased, small fluxes were still observed well after 18:00 when large changes in $\delta^{18}\text{O}$ and
500 d_v were observed. Hence, as I_{ET} was positive and negative for $\delta^{18}\text{O}$ and D-excess, respectively,
501 small ET fluxes into a poorly mixed surface layer could have caused the observed changes.

502 During the night, dew fall caused $\delta^2\text{H}$ and $\delta^{18}\text{O}$ to decrease as heavy isotopes were removed in
503 condensation, especially during the dry period when greater surface cooling was observed.
504 However, dew formation is an equilibrium processes so did not affect d_v . Composites of dry and
505 wet period nocturnal d_v measurements do not show clear nocturnal trends, but individual nights
506 showed considerable variability. A regression of nocturnal d_v with radon concentrations
507 produced a significant negative relationship ($p < 0.001$, $R^2 = 0.31$), indicating that atmospheric
508 stability has some control over nocturnal d_v . High radon is associated with the most stable
509 atmospheres, enhancing the effect of surface exchange in the early evening and inhibiting mixing
510 with the residual layer. Low radon on the other hand, is associated with periods of atmospheric
511 turbulence in which moisture above the nocturnal inversion with a high d_v is mixed down
512 towards the surface.

513

514 **4 Discussion**

515 As has been previously observed (Steen-Larsen et al. 2013; Welp et al. 2012) and predicted by
516 isotopic models (Gat, 1996), our observations showed water vapour $\delta^2\text{H}$ and $\delta^{18}\text{O}$ are controlled
517 by different atmospheric and hydrological processes than d_v . The diurnal cycle was the dominant
518 mode of variability for d_v , consistent with previous studies for a range of ecosystems (Simonin et
519 al. 2014; Welp et al. 2012; Zhao et al. 2014). However, results showed that D-excess variability
520 was controlled by local meteorological conditions and surface exchange at night, ABL growth
521 and decay during transitional periods between the nocturnal and convective ABL, and larger
522 scale processes in the middle of the day.

523 **4.1 Entrainment and d_v diurnal cycle**

524 The Radon measurements showed when the depth of the ABL was rapidly changing through the
525 morning and evening transitions, entrainment from the residual layer and ET fluxes into a rapidly
526 decaying convective boundary layer caused the observed d_v diurnal cycle. Between these
527 transitions, when mixing extends to the capping inversion, entrainment fluxes introduce an
528 additional moisture source from the free troposphere that could modify surface vapour isotopic
529 compositions. **Air above the ABL is drier and moisture is more depleted than at the surface.**
530 **Drying and depleting trends for water vapour, $\delta^2\text{H}$ and $\delta^{18}\text{O}$ throughout the day, particularly**
531 **during the dry period (Figure 8), indicate an important role for entrainment from the free**
532 **troposphere.** Whether this moisture flux impacts on d_v is less clear as it remained reasonably
533 stable once a maximum was reached after the morning transition period. The sign of the
534 isoforcing of moisture entrained from the free troposphere is uncertain, as few free tropospheric

535 d_v measurements exist (He and Smith, 1999; Samuels-Crow et al., 2014). Nevertheless, d_v values
536 did not show a clear trend until vertical mixing began decaying later in the afternoon, so free
537 tropospheric d_v probably had a similar value to moisture already residing in the ABL.

538 **4.2 Remote hydrometeorological processes**

539 While the main focus of this study was to examine the role of local land-atmosphere exchange
540 for the diurnal variability of d_v , the synoptic context of measurements warrants further
541 examination for comparison against previous studies. The slope for the relationship between
542 daytime RH and d_v ($-0.52\%.\%^{-1}$, Table 1) was similar to those determined for measurements
543 over the Mediterranean sea and different ocean basins (between -0.43 and $-0.53\%.\%^{-1}$) (Kurita,
544 2011; Pfahl and Wernli, 2008; Steen-Larsen et al. 2014, 2015; Uemura et al. 2008). Aemisegger
545 *et al.* (2014) showed that this robust relationship is not restricted to coastal locations or
546 measurements over the ocean surface. Using a trajectory model to investigate continental
547 moisture recycling in Europe, they found a similar relationship between d_v and RH of remote
548 moisture sources during the cold season ($-0.57\%.\%^{-1}$), but not the warm season. They concluded
549 moisture recycling is weakest during winter, causing d_v to retain the signature of vapour
550 evaporated from oceanic moisture sources, but in summer moisture recycling increased and
551 attenuated the relationship. Similarities with their winter data, indicates our daytime d_v
552 measurements were at least partly determined by RH at the oceanic moisture source.

553 Along an air masses back trajectory, entrainment fluxes from the free troposphere could be a
554 major driver of daytime d_v variability. Mixing of warm dry air down to the surface, presumably
555 with a relatively high D-excess (He and Smith, 1999; Samuels-Crow et al., 2014), would give the
556 same negative relationship between d_v and RH observed here. However, for a strong relationship

557 between d_v and RH, there must be a dominant moisture source. For the fraction of entrained air
558 in the ABL to cause the strong linear relationship, the D-excess of vapour and RH in both the
559 ABL and free troposphere must be reasonably constant, as in a two source mixing model.
560 Considering the variability of synoptic scale weather patterns observed (section 3.1), this seems
561 unlikely. Thus, while we cannot definitively rule out the importance of entrainment along back
562 trajectories, it seems more likely that the d_v vs RH relationship was derived from a large
563 unchanging moisture source such as the ocean.

564 A practical application of the d_v vs RH relationship introduced by Aemisegger *et al.* (2014) was
565 to determine the D-excess of the liquid moisture source. Based on the closure assumption of
566 Merlivat and Jouzel (1979), it was shown when RH is 100%, d_v is equal to the D-excess of the
567 liquid moisture source. If between the point of evaporation and measurement location no further
568 kinetic fractionation or mixing of vapour with a different d_v /RH ratio occurred, extrapolating the
569 regression between d_v and RH to 100% RH gives an estimate of moisture source D-excess. For
570 our measurements a value of -8‰ was determined, remarkably similar to the D-excess
571 determined for ocean water off the east coast of Australia by Xu *et al.* (2012) using a global
572 ocean model. In contrast to recent literature (Simonin *et al.* 2014; Welp *et al.* 2012; Zhao *et al.*
573 2014), this suggests that although the common diurnal cycle was observed, daytime observations
574 are potentially a tracer of RH at the oceanic moisture source, but it is likely restricted to periods
575 when moisture recycling is weak.

576 Whilst we have shown a relationship between the RH and d_v consistent with an oceanic vapour
577 source, the consistency of the relationship over longer time periods is uncertain. Indeed, it may
578 be the reason we show a strong relationship where Welp *et al.* (2012) did not for longer datasets

579 from six mid-latitude sites in China and the USA. As pointed out earlier, lower slopes and
580 weaker relationships result from stronger moisture recycling, which indicates moisture recycling
581 and soil moisture state may be the most important variable controlling the relationship between
582 d_v and RH. Here we present data from after an extended dry period, where the dominant moisture
583 source is the ocean surrounding the Australian continent. So during wetter periods, increase in
584 the local and remote moisture recycling probably weakens the relationship between local d_v and
585 RH (Aemisegger et al. 2014). However, for locations such as semi-arid Australia where extended
586 dry periods prevail, the relationship between d_v and RH may be reasonably robust and prevail as
587 a tracer of oceanic evaporative environments.

588 **4.3 Controls of d_{ET}**

589 The chamber d_{ET} measurements showed ET fluxes imposed a negative isoforcing on d_v , in
590 contrast to interpretations in previous studies investigating d_v variability on diurnal time scales
591 (Simonin et al. 2014; Zhao et al. 2014). However, it is expected that the sign and magnitude of
592 the D-excess isoforcing would vary both spatially and temporally, in particular with soil moisture
593 state. After a rain event, soil moisture D-excess would decrease following a pseudo-Rayleigh
594 process (Barnes and Allison, 1988). Therefore, immediately after a rainfall event, d_{ET} would be
595 higher and probably impose a positive isoforcing. Here the negative d_{ET} caused the d_v to decrease
596 rapidly as convective mixing shutdown. When isoforcing is positive after a rain event, the
597 diurnal cycle observed here and elsewhere therefore may not be observed. Although
598 equilibration between liquid and vapour pools, as alluded to by Simonin *et al.*, (2014), may still
599 help maintain observed trends. As soil dries, a tipping point when the ET fluxes switch from
600 positive to negative isoforcing will be observed. This has implications for studies attempting to

601 use d_v as a tracer of continental moisture recycling, as the large spatial variability of rainfall and
602 the associated soil moisture state would lead to large spatial and temporal variability for d_{ET} .
603 Although, the strongest moisture recycling is expected for wet soils when d_{ET} is higher, spatial
604 and temporal variability in d_{ET} would still be important.

605 Relative magnitudes of evaporation and transpiration fluxes are important for d_{ET} , as the two
606 processes could have different D-excess values and could vary strongly between precipitation or
607 irrigation events. The classical view of ET isotope fluxes is transpiration has an isotopic
608 composition closer to the source moisture than evaporation, so a higher D-excess. However,
609 greater fractionation of the evaporation source pool causes its D-excess value to decrease over
610 time, causing D-excess of two process to converge. The impact of converging isotopic signatures
611 for ET component fluxes on moisture recycling would depend on the land surface type, but
612 would constitute an important variable influencing the D-excess of local and remote moisture
613 recycling. Further studies investigating how ET partitioning and drying of soil moisture
614 reservoirs following irrigation or precipitation events would lead to a better understanding of
615 how moisture recycling influences the ambient d_v on continental and local scales.

616 **5 Conclusions**

617 To determine how local ET fluxes modified water vapour D-excess, in-situ observations were
618 collected in a semi-arid region of south-eastern Australia. The diurnal cycle exhibited high
619 values during the day and low values at night, reflected findings from previous studies. With
620 chamber based measurements of isotopic compositions in evaporative fluxes, it was shown local
621 ET fluxes exhibited a negative forcing on the ambient water vapour D-excess that could not

622 explain the high daytime values. A strong negative relationship was observed between the locally
623 measured relative humidity and vapour D-excess during the daytime, consistent with
624 relationships observed for oceanic moisture sources. **During the evening transition, collapse of**
625 **the convective boundary layer and small ET fluxes with negative D-excess isoforcing were**
626 **responsible for lowering the D-excess of water vapour near the surface.** In addition, a negative
627 nocturnal correlation between D-excess in water vapour and radon concentrations indicated
628 transient nocturnal mixing events shifted the D-excess back towards the higher values observed
629 during the day, with the most stable (least turbulent) nights producing the lowest D-excess
630 values. In the morning, encroachment and entrainment of high D-excess air from above caused
631 D-excess of surface vapour to increase back to the synoptic values.

632 Overall, it was found that the magnitude of the D-excess diurnal cycle was controlled
633 predominantly by interplay between synoptic forcing and local ABL processes and was modified
634 further by nocturnal surface exchange processes and turbulent mixing. The low D-excess of the
635 ET fluxes determined from flux chambers in this study illustrated that the impact of large scale
636 moisture recycling may be both spatially and temporally variable, depending on the soil moisture
637 state. This has implications for studies using D-excess to investigate moisture recycling.

638 **6 Acknowledgements**

639 Stephen Parkes was supported by the Atmospheric Mixing and Pollution Transport (AMPT)
640 project at the Australian Nuclear Science and Technology Organization (ANSTO). The Baldry
641 Hydrological Observatory field campaign was supported by Australian Research Council
642 Discovery grants DP0987478 and DP120104718. Matthew McCabe and Stephen Parkes
643 acknowledge the support of the King Abdullah University of Science and Technology. We thank

644 Peter Graham, Cecilia Azcurra, Dr. Jin Wang and Yingzhe Cai for their assistance during the
645 campaign. We also appreciate the support of Diana and Jason Tremain for access to the Baldry
646 Hydrological Observatory and surrounding farmland, Chris Dimovski for performing plant and
647 soil water extractions, and Barbara Neklapilova analysis of plant and soil water samples.

648 For access to the data used in this paper contact Dr Stephen Parkes by email
649 (stephen.parkes@kaust.edu.sa).

650

651

652 7 References

653 Aemisegger, F., Pfahl, S., Sodemann, H., Lehner, I., Seneviratne, S. I. and Wernli, H.:
654 Deuterium excess as a proxy for continental moisture recycling and plant transpiration, *Atmos.*
655 *Chem. Phys.*, 14(8), 4029–4054, doi:10.5194/acp-14-4029-2014, 2014.

656 Allison, G. B., Barnes, C. J. and Hughes, M. W.: The distribution of deuterium and ^{18}O in dry
657 soils 2. Experimental, *J. Hydrol.*, 64(1-4), 377–397, doi:10.1016/0022-1694(83)90078-1, 1983.

658 Barnes, C. J. and Allison, G. B.: Tracing of water movement in the unsaturated zone using stable
659 isotopes of hydrogen and oxygen, *J. Hydrol.*, 100(1-3), 143–176, doi:10.1016/0022-
660 1694(88)90184-9, 1988.

661 Bastrikov, V., Steen-Larsen, H. C., Masson-Delmotte, V., Griбанov, K., Cattani, O., Jouzel, J.
662 and Zakharov, V.: Continuous measurements of atmospheric water vapour isotopes in western
663 Siberia (Kourovka), *Atmos. Meas. Tech.*, 7(6), 1763–1776, doi:10.5194/amt-7-1763-2014, 2014.

664 Berkelhammer, M., Hu, J., Bailey, A., Noone, D. C., Still, C. J., Barnard, H., Gochis, D., Hsiao,
665 G. S., Rahn, T. and Turnipseed, A.: The nocturnal water cycle in an open-canopy forest, *J.*
666 *Geophys. Res. Atmos.*, 118(17), 10,210–225,242, doi:10.1002/jgrd.50701, 2013.

667 Chambers, S. D., Wang, F., Williams, A. G., Xiaodong, D., Zhang, H., Lonati, G., Crawford, J.,
668 Griffiths, A. D., Ianniello, A. and Allegrini, I.: Quantifying the influences of atmospheric
669 stability on air pollution in Lanzhou, China, using a radon-based stability monitor, *Atmos.*
670 *Environ.*, 107, 233–243, doi:10.1016/j.atmosenv.2015.02.016, 2015a.

671 Chambers, S. D., Williams, A. G., Crawford, J. and Griffiths, A. D.: On the use of radon for
672 quantifying the effects of atmospheric stability on urban emissions, *Atmos. Chem. Phys.*
673 *Discuss.*, 14(18), 25411–25452, doi:10.5194/acpd-14-25411-2014, 2014.

674 Chambers, S. D., Williams, A. G., Crawford, J. and Griffiths, A. D.: On the use of radon for
675 quantifying the effects of atmospheric stability on urban emissions, *Atmos. Chem. Phys.*, 15(3),
676 1175–1190, doi:10.5194/acp-15-1175-2015, 2015b.

677 Craig, H.: Isotopic Variations in Meteoric Waters, *Sci.*, 133 (3465), 1702–1703,
678 doi:10.1126/science.133.3465.1702, 1961.

679 Craig, H. and Gordon, L. I.: Deuterium and oxygen-18 variations in the ocean and marine
680 atmosphere, in *Stable isotopes in oceanographic studies and paleotemperatures*, Proceedings,
681 Spoleto, Italy., edited by E. Tongiogi, pp. 9–130, Pisa, Italy., 1965.

682 Crawford, J., Hughes, C. E. and Parkes, S. D.: Is the isotopic composition of event based
683 precipitation driven by moisture source or synoptic scale weather in the Sydney Basin,
684 Australia?, *J. Hydrol.*, 507(0), 213–226, doi:http://dx.doi.org/10.1016/j.jhydrol.2013.10.031,
685 2013.

686 Dansgaard, W.: Stable isotopes in precipitation, *Tellus*, 16(4), 436–468, doi:10.1111/j.2153-
687 3490.1964.tb00181.x, 1964.

688 Decker, M., Pitman, A. and Evans, J.: Diagnosing the seasonal land–atmosphere correspondence
689 over northern Australia: dependence on soil moisture state and correspondence strength
690 definition, *Hydrol. Earth Syst. Sci.*, 19(8), 3433–3447, doi:10.5194/hess-19-3433-2015, 2015.

691 Dubbert, M., Cuntz, M., Piayda, A., Maguás, C. and Werner, C.: Partitioning evapotranspiration
692 – Testing the Craig and Gordon model with field measurements of oxygen isotope ratios of
693 evaporative fluxes, *J. Hydrol.*, 496, 142–153, doi:10.1016/j.jhydrol.2013.05.033, 2013.

694 Evans, J. P. and McCabe, M. F.: Regional climate simulation over Australia’s Murray-Darling
695 basin: A multitemporal assessment, *J. Geophys. Res. Atmos.*, 115(D14), n/a–n/a,
696 doi:10.1029/2010JD013816, 2010.

697 Finnigan, J. J., Clement, R., Malhi, Y., Leuning, R. and Cleugh, H. A.: A Re-Evaluation of
698 Long-Term Flux Measurement Techniques Part I: Averaging and Coordinate Rotation,
699 *Boundary-Layer Meteorol.*, 107(1), 1–48, doi:10.1023/A:1021554900225, 2003.

700 Froehlich, K., Kralik, M., Papesch, W., Rank, D., Scheifinger, H. and Stichler, W.: Deuterium
701 excess in precipitation of Alpine regions – moisture recycling, *Isotopes Environ. Health Stud.*,
702 44(1), 61–70, doi:10.1080/10256010801887208, 2008.

703 Gat, J. R.: OXYGEN AND HYDROGEN ISOTOPES IN THE HYDROLOGIC CYCLE, *Annu.*
704 *Rev. Earth Planet. Sci.*, 24(1), 225–262, doi:10.1146/annurev.earth.24.1.225, 1996.

705 Gat, J. R., Bowser, C. J. and Kendall, C.: The contribution of evaporation from the Great Lakes
706 to the continental atmosphere: estimate based on stable isotope data, *Geophys. Res. Lett.*, 21(7),
707 557–560, doi:10.1029/94GL00069, 1994.

708 Gat, J. R., Klein, B., Kushnir, Y., Roether, W., Wernli, H., Yam, R. and Shemesh, A.: Isotope
709 composition of air moisture over the Mediterranean Sea: an index of the air–sea interaction
710 pattern, *Tellus B*, 55(5), 953–965, doi:10.1034/j.1600-0889.2003.00081.x, 2003.

711 Griffiths, A. D., Parkes, S. D., Chambers, S. D., McCabe, M. F. and Williams, A. G.: Improved
712 mixing height monitoring through a combination of lidar and radon measurements, *Atmos.*
713 *Meas. Tech.*, 6(2), 207–218, doi:10.5194/amt-6-207-2013, 2013.

- 714 Harding, K. J. and Snyder, P. K.: Modeling the Atmospheric Response to Irrigation in the Great
715 Plains. Part I: General Impacts on Precipitation and the Energy Budget, *J. Hydrometeorol.*, 13(6),
716 1667–1686, doi:10.1175/JHM-D-11-098.1, 2012.
- 717 He, H. and Smith, R. B.: Stable isotope composition of water vapor in the atmospheric boundary
718 layer above the forests of New England, *J. Geophys. Res. Atmos.*, 104(D9), 11657–11673,
719 doi:10.1029/1999JD900080, 1999.
- 720 Horita, J. and Wesolowski, D. J.: Liquid-vapor fractionation of oxygen and hydrogen isotopes of
721 water from the freezing to the critical temperature, *Geochim. Cosmochim. Acta*, 58(16), 3425–
722 3437, doi:http://dx.doi.org/10.1016/0016-7037(94)90096-5, 1994.
- 723 Huang, L. and Wen, X.: Temporal variations of atmospheric water vapor δD and $\delta^{18}O$ above an
724 arid artificial oasis cropland in the Heihe River Basin, *J. Geophys. Res. Atmos.*, 119(19),
725 2014JD021891, doi:10.1002/2014JD021891, 2014.
- 726 Hughes, C. E. and Crawford, J.: Spatial and temporal variation in precipitation isotopes in the
727 Sydney Basin, Australia, *J. Hydrol.*, 489(0), 42–55,
728 doi:http://dx.doi.org/10.1016/j.jhydrol.2013.02.036, 2013.
- 729 Jana, R. B., Ershadi, A. and McCabe, M. F.: Examining the relationship between intermediate
730 scale soil moisture and terrestrial evaporation within a semi-arid grassland, *Hydrol. Earth Syst.*
731 *Sci. Discuss.*, 2016, 1–27, doi:10.5194/hess-2016-186, 2016.
- 732 Keeling, C. D.: The concentration and isotopic abundances of atmospheric carbon dioxide in
733 rural areas, *Geochim. Cosmochim. Acta*, 13(4), 322–334, doi:10.1016/0016-7037(58)90033-4,
734 1958.
- 735 Kurita, N.: Origin of Arctic water vapor during the ice-growth season, *Geophys. Res. Lett.*,
736 38(2), n/a–n/a, doi:10.1029/2010GL046064, 2011.
- 737 Lai, C.-T. and Ehleringer, J.: Deuterium excess reveals diurnal sources of water vapor in forest
738 air, *Oecologia*, 165(1), 213–223, doi:10.1007/s00442-010-1721-2, 2011.
- 739 Lee, X., Griffis, T. J., Baker, J. M., Billmark, K. A., Kim, K. and Welp, L. R.: Canopy-scale
740 kinetic fractionation of atmospheric carbon dioxide and water vapor isotopes, *Global*
741 *Biogeochem. Cycles*, 23(1), GB1002, doi:10.1029/2008GB003331, 2009.
- 742 Leuning, R.: The correct form of the Webb, Pearman and Leuning equation for eddy fluxes of
743 trace gases in steady and non-steady state, horizontally homogeneous flows, *Boundary-Layer*
744 *Meteorol.*, 123(2), 263–267, doi:10.1007/s10546-006-9138-5, 2007.
- 745 Lin, J. C., Gerbig, C., Wofsy, S. C., Andrews, A. E., Daube, B. C., Davis, K. J. and Grainger, C.
746 A.: A near-field tool for simulating the upstream influence of atmospheric observations: The
747 Stochastic Time-Inverted Lagrangian Transport (STILT) model, *J. Geophys. Res.*, 108, 4493,
748 doi:10.1029/2002JD003161, 2003.
- 749 Lu, X., Liang, L. L., Wang, L., Jenerette, G. D., McCabe, M. F. and Grantz, D. A.: Partitioning
750 of evapotranspiration using a stable isotope technique in an arid and high temperature
751 agricultural production system, *Agric. Water Manag.*, In Press, ,
752 doi:http://dx.doi.org/10.1016/j.agwat.2016.08.012, 2016.
- 753 Masson-Delmotte, V., Jouzel, J., Landais, A., Stievenard, M., Johnsen, S. J., White, J. W. C.,

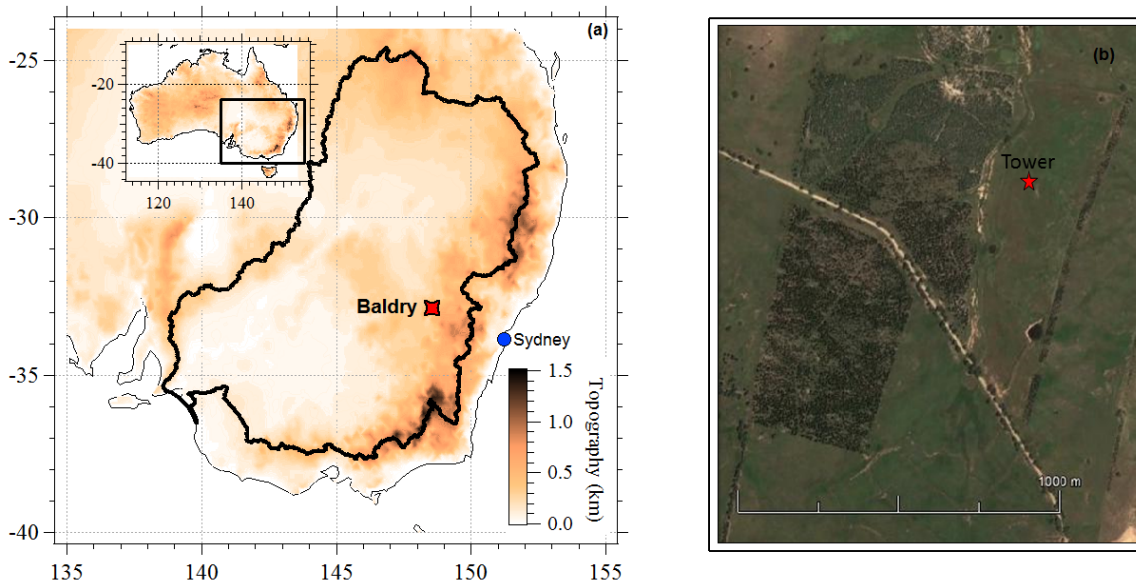
- 754 Werner, M., Sveinbjörnsdóttir, A. and Fuhrer, K.: GRIP Deuterium Excess Reveals Rapid and
755 Orbital-Scale Changes in Greenland Moisture Origin, *Sci.*, 309 (5731), 118–121,
756 doi:10.1126/science.1108575, 2005.
- 757 Mathieu, R. and Bariac, T.: A numerical model for the simulation of stable isotope profiles in
758 drying soils, *J. Geophys. Res. Atmos.*, 101(D7), 12685–12696, doi:10.1029/96JD00223, 1996.
- 759 McCabe, M. F., Ershadi, A., Jimenez, C., Miralles, D. G., Michel, D. and Wood, E. F.: The
760 GEWEX LandFlux project: evaluation of model evaporation using tower-based and globally
761 gridded forcing data, *Geosci. Model Dev.*, 9(1), 283–305, doi:10.5194/gmd-9-283-2016, 2016.
- 762 Merlivat, L.: Molecular diffusivities of H₂O¹⁶O, HD¹⁶O, and H₂¹⁸O in gases, *J. Chem. Phys.*,
763 69(6), 2864, doi:10.1063/1.436884, 1978.
- 764 Merlivat, L. and Jouzel, J.: Global climatic interpretation of the deuterium-oxygen 18
765 relationship for precipitation, *J. Geophys. Res. Ocean.*, 84(C8), 5029–5033,
766 doi:10.1029/JC084iC08p05029, 1979.
- 767 Noone, D., Risi, C., Bailey, A., Berkelhammer, M., Brown, D. P., Buening, N., Gregory, S.,
768 Nusbaumer, J., Schneider, D., Sykes, J., Vanderwende, B., Wong, J., Meillier, Y. and Wolfe, D.:
769 Determining water sources in the boundary layer from tall tower profiles of water vapor and
770 surface water isotope ratios after a snowstorm in Colorado, *Atmos. Chem. Phys.*, 13(3), 1607–
771 1623, doi:10.5194/acp-13-1607-2013, 2013.
- 772 Pfahl, S. and Wernli, H.: Air parcel trajectory analysis of stable isotopes in water vapor in the
773 eastern Mediterranean, *J. Geophys. Res. Atmos.*, 113(D20), n/a–n/a,
774 doi:10.1029/2008JD009839, 2008.
- 775 Pfahl, S. and Wernli, H.: Lagrangian simulations of stable isotopes in water vapor: An evaluation
776 of nonequilibrium fractionation in the Craig-Gordon model, *J. Geophys. Res. Atmos.*, 114(D20),
777 D20108, doi:10.1029/2009JD012054, 2009.
- 778 Risi, C., Noone, D., Frankenberg, C. and Worden, J.: Role of continental recycling in
779 intraseasonal variations of continental moisture as deduced from model simulations and water
780 vapor isotopic measurements, *Water Resour. Res.*, 49(7), 4136–4156, doi:10.1002/wrcr.20312,
781 2013.
- 782 Samuels-Crow, K. E., Galewsky, J., Sharp, Z. D. and Dennis, K. J.: Deuterium-excess in
783 subtropical free troposphere water vapor: continuous measurements from the Chajnantor Plateau,
784 northern Chile, *Geophys. Res. Lett.*, 2014GL062302, doi:10.1002/2014GL062302, 2014.
- 785 Simonin, K. A., Link, P., Rempe, D., Miller, S., Oshun, J., Bode, C., Dietrich, W. E., Fung, I.
786 and Dawson, T. E.: Vegetation induced changes in the stable isotope composition of near surface
787 humidity, *Ecohydrology*, 7(3), 936–949, doi:10.1002/eco.1420, 2014.
- 788 Steen-Larsen, H. C., Johnsen, S. J., Masson-Delmotte, V., Stenni, B., Risi, C., Sodemann, H.,
789 Balslev-Clausen, D., Blunier, T., Dahl-Jensen, D., Ellehøj, M. D., Falourd, S., Grindsted, A.,
790 Gkinis, V., Jouzel, J., Popp, T., Sheldon, S., Simonsen, S. B., Sjolte, J., Steffensen, J. P.,
791 Sperlich, P., Sveinbjörnsdóttir, A. E., Vinther, B. M. and White, J. W. C.: Continuous monitoring
792 of summer surface water vapor isotopic composition above the Greenland Ice Sheet, *Atmos.*
793 *Chem. Phys.*, 13(9), 4815–4828, doi:10.5194/acp-13-4815-2013, 2013.
- 794 Steen-Larsen, H. C., Sveinbjörnsdóttir, A. E., Jonsson, T., Ritter, F., Bonne, J.-L., Masson-

- 795 Delmotte, V., Sodemann, H., Blunier, T., Dahl-Jensen, D. and Vinther, B. M.: Moisture sources
796 and synoptic to seasonal variability of North Atlantic water vapor isotopic composition, *J.*
797 *Geophys. Res. Atmos.*, 120(12), 2015JD023234, doi:10.1002/2015JD023234, 2015.
- 798 Steen-Larsen, H. C., Sveinbjörnsdóttir, A. E., Peters, A. J., Masson-Delmotte, V., Guishard, M.
799 P., Hsiao, G., Jouzel, J., Noone, D., Warren, J. K. and White, J. W. C.: Climatic controls on
800 water vapor deuterium excess in the marine boundary layer of the North Atlantic based on 500
801 days of in situ, continuous measurements, *Atmos. Chem. Phys.*, 14(15), 7741–7756,
802 doi:10.5194/acp-14-7741-2014, 2014.
- 803 Tian, L., Masson-Delmotte, V., Stievenard, M., Yao, T. and Jouzel, J.: Tibetan Plateau summer
804 monsoon northward extent revealed by measurements of water stable isotopes, *J. Geophys. Res.*
805 *Atmos.*, 106(D22), 28081–28088, doi:10.1029/2001JD900186, 2001.
- 806 Uemura, R., Matsui, Y., Yoshimura, K., Motoyama, H. and Yoshida, N.: Evidence of deuterium
807 excess in water vapor as an indicator of ocean surface conditions, *J. Geophys. Res. Atmos.*,
808 113(D19), n/a–n/a, doi:10.1029/2008JD010209, 2008.
- 809 Vallet-Coulomb, C., Gasse, F. and Sonzogni, C.: Seasonal evolution of the isotopic composition
810 of atmospheric water vapour above a tropical lake: Deuterium excess and implication for water
811 recycling, *Geochim. Cosmochim. Acta*, 72(19), 4661–4674, doi:10.1016/j.gca.2008.06.025,
812 2008.
- 813 Wang, L., Niu, S., Good, S. P., Soderberg, K., McCabe, M. F., Sherry, R. A., Luo, Y., Zhou, X.,
814 Xia, J. and Caylor, K. K.: The effect of warming on grassland evapotranspiration partitioning
815 using laser-based isotope monitoring techniques, *Geochim. Cosmochim. Acta*, 111, 28–38,
816 doi:10.1016/j.gca.2012.12.047, 2013a.
- 817 Wang, L., Niu, S., Good, S. P., Soderberg, K., McCabe, M. F., Sherry, R. A., Luo, Y., Zhou, X.,
818 Xia, J. and Caylor, K. K.: The effect of warming on grassland evapotranspiration partitioning
819 using laser-based isotope monitoring techniques, *Geochim. Cosmochim. Acta*, 111, 28–38,
820 doi:http://dx.doi.org/10.1016/j.gca.2012.12.047, 2013b.
- 821 Wei, J., Dirmeyer, P. A., Wisser, D., Bosilovich, M. G. and Mocko, D. M.: Where Does the
822 Irrigation Water Go? An Estimate of the Contribution of Irrigation to Precipitation Using
823 MERRA, *J. Hydrometeorol.*, 14(1), 275–289, doi:10.1175/JHM-D-12-079.1, 2012.
- 824 Welp, L. R., Lee, X., Griffis, T. J., Wen, X.-F., Xiao, W., Li, S., Sun, X., Hu, Z., Val Martin, M.
825 and Huang, J.: A meta-analysis of water vapor deuterium-excess in the midlatitude atmospheric
826 surface layer, *Global Biogeochem. Cycles*, 26(3), GB3021, doi:10.1029/2011GB004246, 2012.
- 827 Williams, A. G., Chambers, S. and Griffiths, A.: Bulk Mixing and Decoupling of the Nocturnal
828 Stable Boundary Layer Characterized Using a Ubiquitous Natural Tracer, *Boundary-Layer*
829 *Meteorol.*, 149(3), 381–402, doi:10.1007/s10546-013-9849-3, 2013.
- 830 Williams, A. G., Zahorowski, W., Chambers, S., Griffiths, A., Hacker, J. M., Element, A. and
831 Werczynski, S.: The Vertical Distribution of Radon in Clear and Cloudy Daytime Terrestrial
832 Boundary Layers, *J. Atmos. Sci.*, 68(1), 155–174, doi:10.1175/2010JAS3576.1, 2010.
- 833 Xu, X., Werner, M., Butzin, M. and Lohmann, G.: Water isotope variations in the global ocean
834 model MPI-OM, *Geosci. Model Dev.*, 5(3), 809–818, doi:10.5194/gmd-5-809-2012, 2012.
- 835 Zahorowski, W., Chambers, S. D. and Henderson-Sellers, A.: Ground based radon-222

836 observations and their application to atmospheric studies, *J. Environ. Radioact.*, 76(1–2), 3–33,
837 doi:<http://dx.doi.org/10.1016/j.jenvrad.2004.03.033>, 2004.

838 Zhao, L., Wang, L., Liu, X., Xiao, H., Ruan, Y. and Zhou, M.: The patterns and implications of
839 diurnal variations in the δ -excess of plant water, shallow soil water and air moisture, *Hydrol.*
840 *Earth Syst. Sci.*, 18(10), 4129–4151, doi:10.5194/hess-18-4129-2014, 2014.

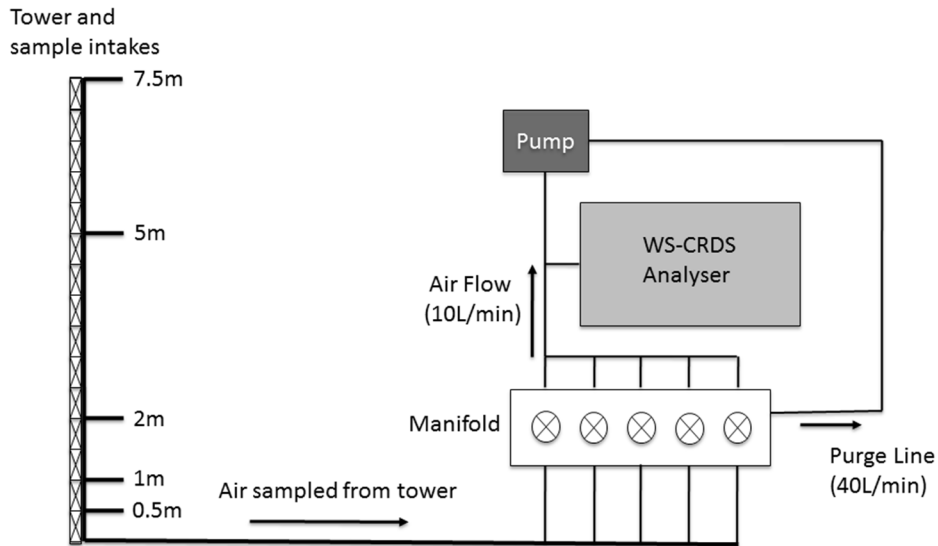
841 8 Figure Captions



842

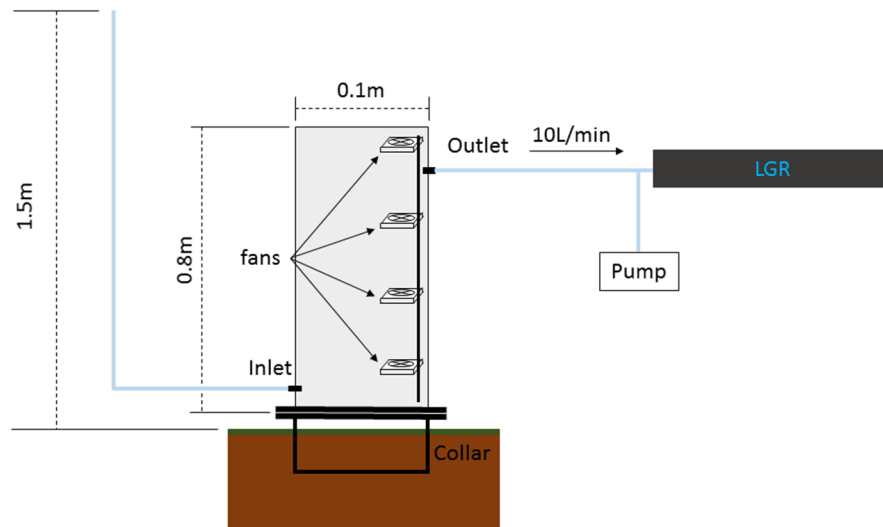
Figure 1: a) Location of the Baldry Hydrological Observatory. The heavy black border outlines the boundary of the Murray-Darling Basin, (b) location of the field site used for the campaign.

843



844

845 Figure 2: Sampling system for the automated in-situ sampling of water vapour isotopes from the
 846 tower.



847

848 Figure 3: Chamber design used for determining isotopic compositions of ET fluxes.

849

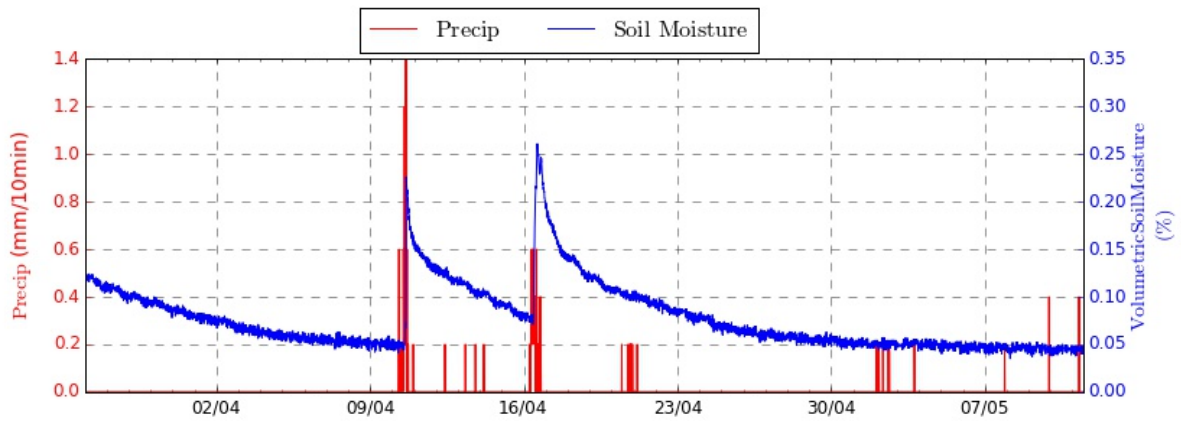
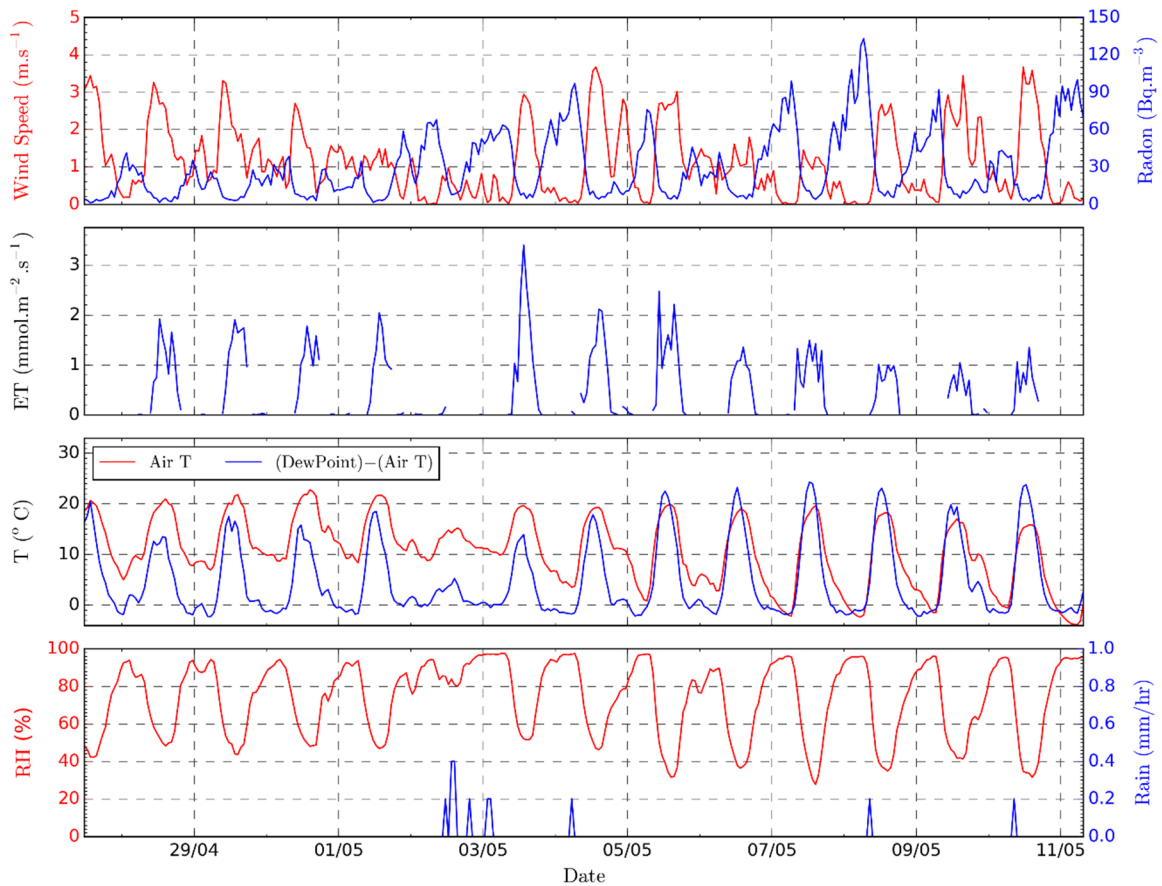


Figure 4: Precipitation and 0-10 cm soil moisture for the month leading up to and including the field campaign.

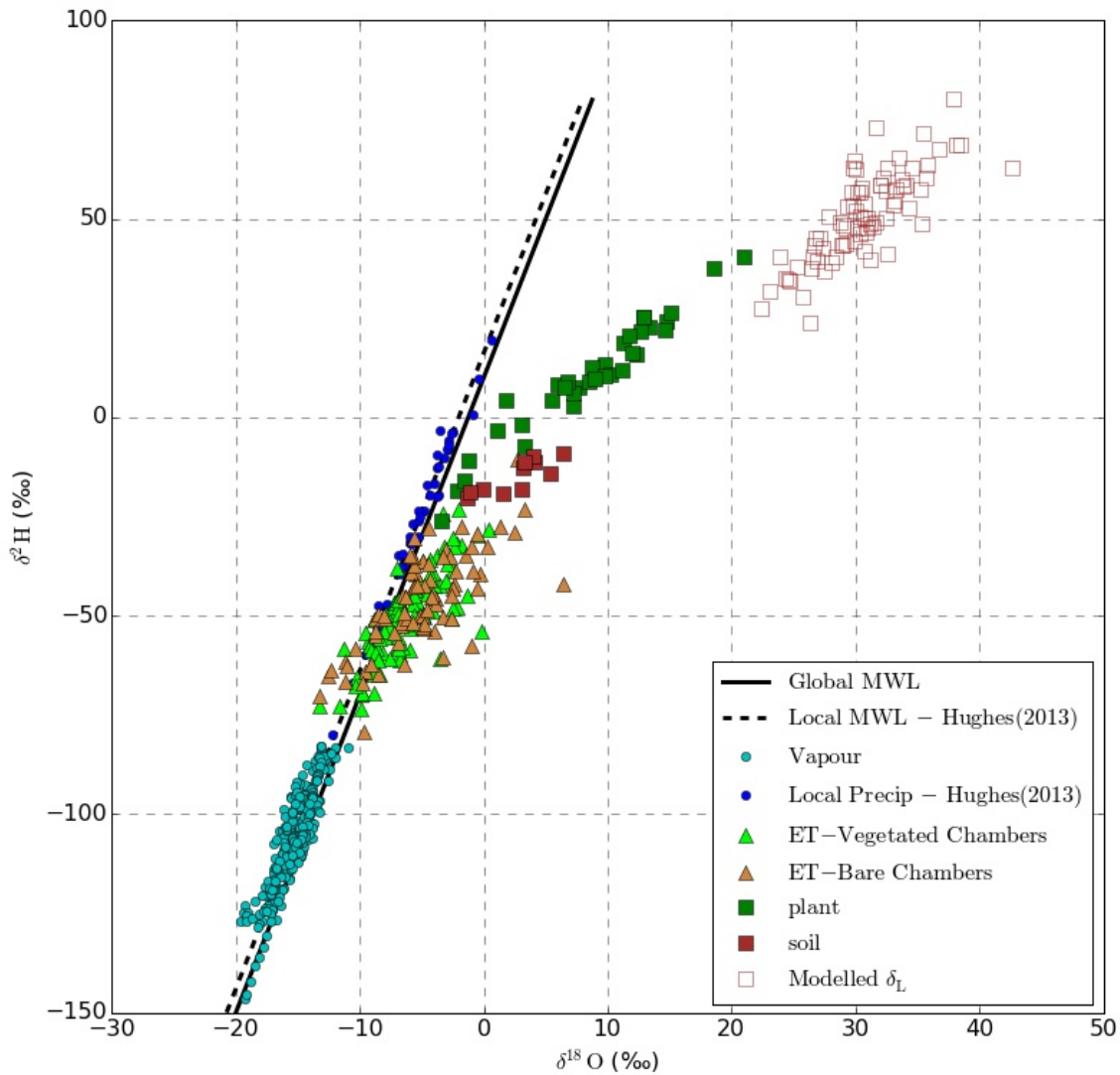
850



851

Figure 5: Meteorological and radon measurements collected throughout the field campaign. Meteorological measurements are block hourly averages calculated from 15-minute observations. Small rain events on the 4th, 8th and 10th May were most likely dew fall rather than precipitation.

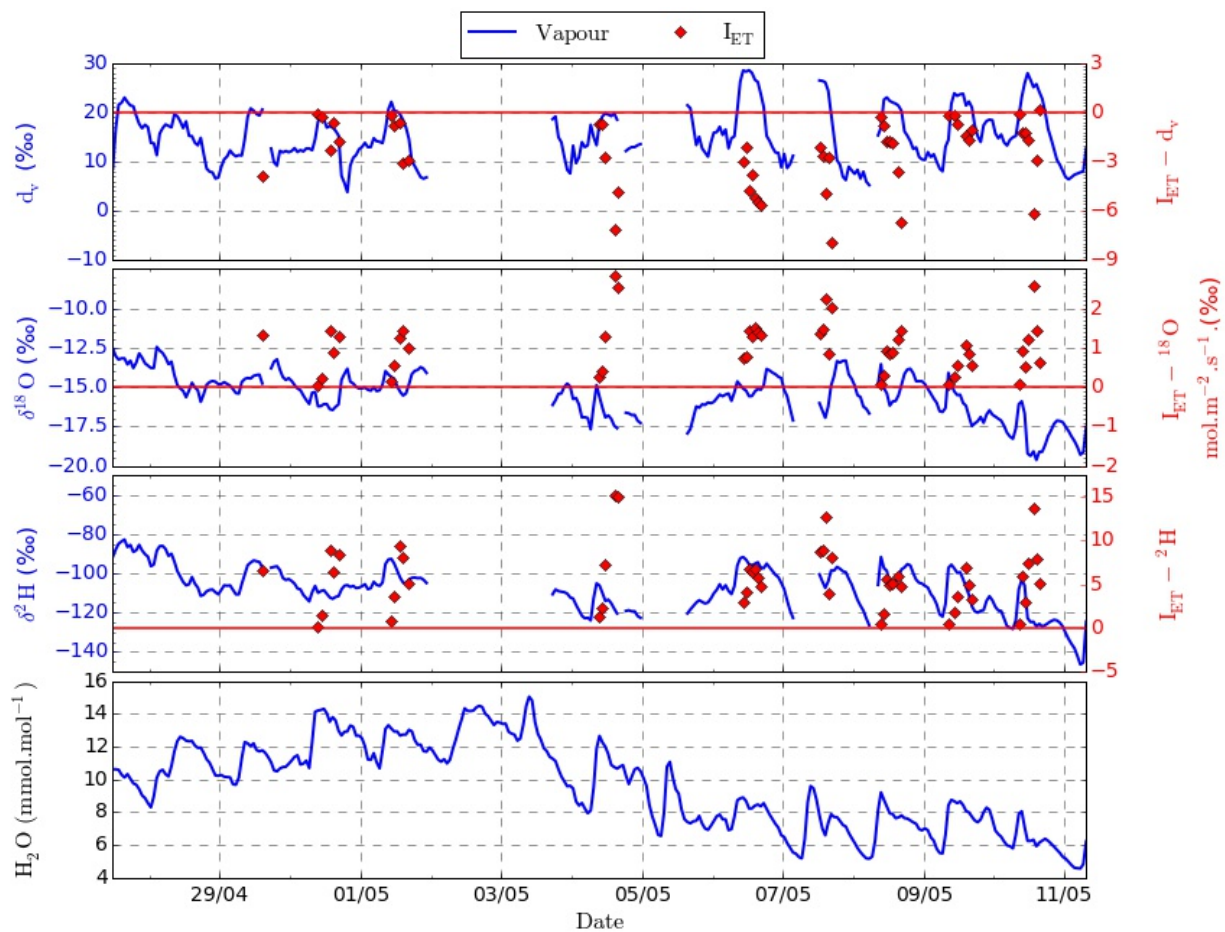
852



853

Figure 6: Relationship between $\delta^{2}\text{H}$ and $\delta^{18}\text{O}$ for observed and modelled water pools. Linear regressions are shown for local and global meteoric water lines (MWL). Data from Hughes and Crawford (2013) are for monthly cumulative rainfall samples between 2005 and 2008.

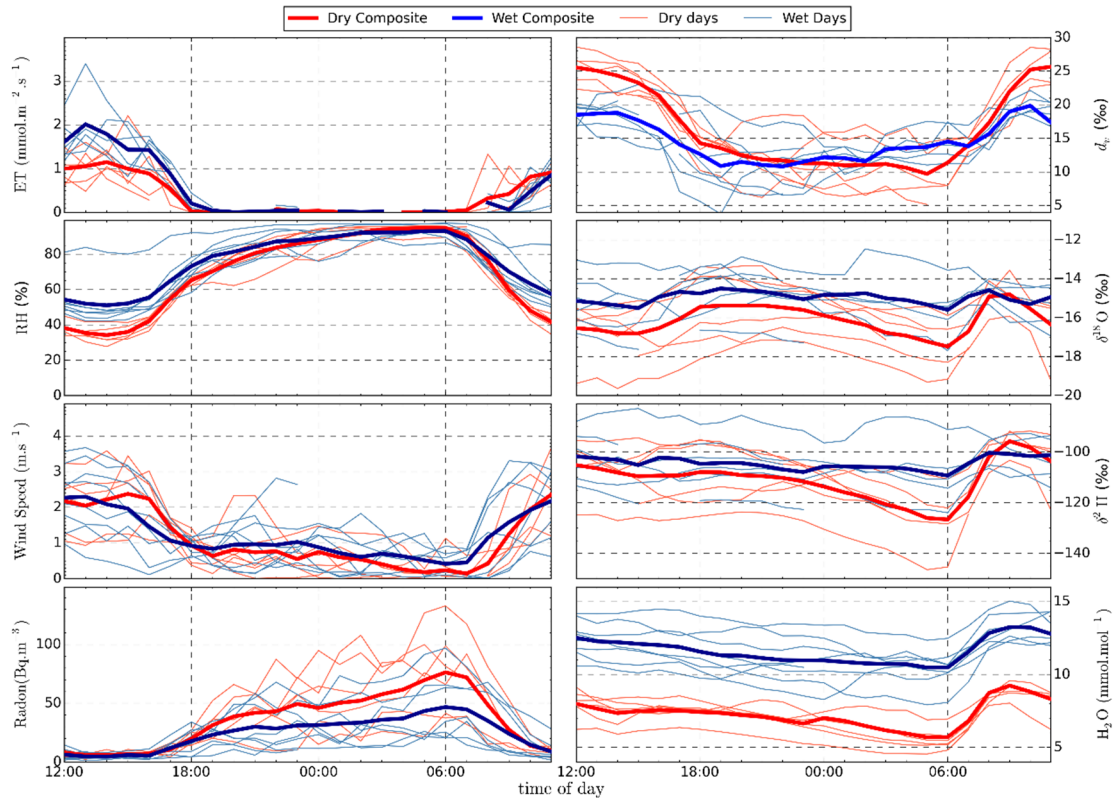
854



855

Figure 7: Time series of hourly water vapour mixing ratio, isotopic composition and ET isoforcing (I_{ET}).

856



857

Figure 8: Data plotted by time of day and divided into dry and wet periods (see text in section 3.5). Diurnal composites are shown for dry (red) and wet (blue) periods.

858

859 Table 1: Correlation between meteorological variables and the isotopic composition of water
 860 vapour. Values outside the brackets are statistics for the hourly observations. Inside the brackets
 861 are correlation statistics for average values calculated between 11:00 and 15:00 LST, hence
 862 representing activity during a convective boundary layer. Significant correlations are shown in
 863 bold; $p < 0.001$ for hourly observations and $p < 0.05$ for the daytime averages (due to the smaller
 864 number of points).

		T	RH	ET	H₂O	I_{ET}^a
δ²H	Slope	0.83 (0.51)	-0.17 (0.23)	1.4 (6.1)	2.1 (0.85)	-1.1 (-3.0)
	Intercept	-120 (-140)	-95 (-110)	-110 (-110)	-110 (-130)	-99 (-83)
	R²	0.24 (0.13)	0.09 (0.02)	0.001 (0.04)	0.2 (0.04)	0.2 (0.45)
	p	<0.001 (0.3)	<0.001 (0.7)	0.32 (0.6)	<0.001 (0.5)	0.002 (0.05)
δ¹⁸O	Slope	0.046 (0.44)	-0.01 (-0.01)	-0.37 (1.8)	0.27 (0.29)	-0.7 (-1.9)
	Intercept	-16 (-24)	-16 (-20)	-15 (-18)	-18 (-19)	-15 (-14)
	R²	0.04 (0.30)	0.004 (0.2)	0.02 (0.16)	0.2 (0.2)	0.14 (0.32)
	p	<0.001 (0.08)	0.26 (0.19)	0.05 (0.26)	<0.001 (0.15)	0.008 (0.11)
d_v	Slope	0.51 (-1.4)	-0.21 (-0.52)	0.01 (-0.16)	0.15 (-1.3)	-1.4 (-2.4)
	Intercept	-9.9 (48)	31 (44)	-15 (-18)	14 (35)	21 (20)
	R²	0.40 (0.48)	0.62 (0.74)	0.22 (0.30)	0.004 (0.71)	0.06 (0.08)
	p	<0.001 (0.02)	<0.001 (<0.01)	0.05 (0.01)	0.26 (<0.01)	0.01 (0.44)

865 ^aIsoforcing correlations were calculated for simultaneous vapour and chamber measurements.
 866 Hourly averaged values were used for both.

867